



Are There Magnetars in High-mass X-Ray Binaries?*

Kun Xu^{1,2,3}, Xiang-Dong Li^{3,4}, Zhe Cui³, Qiao-Chu Li^{3,4}, Yong Shao^{3,4}, Xilong Liang^{1,2}, and Jifeng Liu^{1,2,5}

¹School of Astronomy and Space Sciences, University of Chinese Academy of Sciences, Beijing 100049, China; xukun@smail.nju.edu.cn

²Key Laboratory of Optical Astronomy, National Astronomical Observatories, Chinese Academy of Sciences, Beijing 100101, China

³Department of Astronomy, Nanjing University, Nanjing 210023, China

⁴Key Laboratory of Modern Astronomy and Astrophysics, Nanjing University, Ministry of Education, Nanjing 210023, China

⁵WHU-NAOC Joint Center for Astronomy, Wuhan University, Wuhan, China

Received 2021 August 17; revised 2021 October 18; accepted 2021 October 20; published 2022 January 21

Abstract

Magnetars form a special population of neutron stars with strong magnetic fields and long spin periods. About 30 magnetars and magnetar candidates known currently are probably isolated, but the possibility that magnetars are in binaries has not been excluded. In this work, we perform spin evolution of neutron stars with different magnetic fields in wind-fed high-mass X-ray binaries and compare the spin period distribution with observations, aiming to find magnetars in binaries. Our simulation shows that some of the neutron stars, which have long spin periods or are in widely-separated systems, need strong magnetic fields to explain their spin evolution. This implies that there are probably magnetars in high-mass X-ray binaries. Moreover, this can further provide a theoretical basis for some unclear astronomical phenomena, such as the possible origin of periodic fast radio bursts from magnetars in binary systems.

Key words: stars: magnetars – stars: neutron – stars: rotation – (stars:) supergiants – accretion – accretion disks – X-rays: binaries

1. Introduction

Magnetars are thought to be a special population of neutron stars (NSs) with magnetic fields $B \gtrsim 10^{14}$ G (Duncan & Thompson 1992; Kaspi & Beloborodov 2017) in general. They pulsate in X-ray band as persistent emission sources with bursts and outbursts, which are powered by their strong magnetic fields (Kaspi & Beloborodov 2017; An & Archibald 2019; Beniamini et al. 2019). However, low-field magnetars were found in observations (Rea et al. 2010; Zhou et al. 2014), and the dipole magnetic field of a few $\times 10^{12}$ G indicates that they are possibly old magnetars (Turolla et al. 2011; Dall’Osso et al. 2012; Tong & Xu 2012). About 30 magnetars and candidates known currently are listed in the McGill Magnetar Catalog⁶ (Olausen & Kaspi 2014) with characteristic magnetic fields from $\sim 6 \times 10^{12}$ to $\sim 2 \times 10^{15}$ G. In addition, some central compact objects (CCOs) may be magnetar candidates, e.g., the one located close to the center of RCW 103 (1E 161 348 –5055) is thought to be a magnetar with $B \gtrsim 5 \times 10^{15}$ G (De Luca et al. 2006; Tong et al. 2016; Ho & Andersson 2017; Xu & Li 2019). All magnetars and candidates are probably isolated NSs (King & Lasota 2019). But in the theory of binary evolution, one cannot exclude the possibility that magnetars are in binaries.

So the question becomes, are there magnetars in binary systems? It seems to be answered when the first ultraluminous X-ray pulsar (ULXP) M82 X-2 was found (Bachetti et al. 2014). The peak luminosity of M82 X-2 is $\sim 10^{40}$ erg s⁻¹, so its magnetic field has been estimated to be $\sim 10^{14}$ G (Eksi et al. 2015; Tsygankov et al. 2016), while other estimation implies that its magnetic field is $\sim 10^{12}$ – 10^{13} G (Dall’Osso et al. 2015; Xu & Li 2017) or even lower ($\lesssim 10^9$ G, Kluzniak & Lasota 2015). Subsequently, more and more ULXPs were discovered but none of them was confirmed to be a magnetar (King & Lasota 2019). However, an interesting idea is that M82 X-2 is an accreting low magnetic field magnetar (Tong 2015; Tong & Wang 2019) with $B \sim 10^{12}$ G (Chen 2017). This is in accord with the current view that the magnetars’ ultrahigh fields decay on a timescale $< 10^5$ – 10^6 yr by Hall drift and Ohmic diffusion (Turolla et al. 2015). After decay, the magnetic fields of old magnetars (or low magnetic field magnetars, or post-magnetars) are on a similar magnitude as that of other pulsars’. Therefore, the problem now is how to pick old magnetars out from the zone of NSs. The long period (~ 2.6 hr) X-ray pulsar in the high-mass X-ray binary (HMXB) 4U 0114+65 provides some inspirations, which could be an old magnetar (Li & van den Heuvel 1999; Sanjurjo-Ferrín et al. 2017) with age of 2.4–5 Myr (Igoshev & Popov 2018). Li & van den Heuvel (1999) thought that it was born as a magnetar and spun down to ~ 10 s by magnetic dipole radiation on a timescale of 10^4 – 10^5 yr, then its magnetosphere started to

* Supported by the National Natural Science Foundation of China.

⁶ The url of the catalog is <http://www.physics.mcgill.ca/~pulsar/magnetar/main.html>.

interact with wind material from the companion and the NS spun down to $\sim 10^4$ s within 10^5 yr. This can lead one to find some clues to the problem in wind-fed HMXBs.

Some mysterious electromagnetic radiations can be interpreted by magnetars in binaries, such as fast radio bursts (FRBs). FRBs are millisecond-duration and extremely bright radio transients (for reviews, see Cordes & Chatterjee 2019; Petroff et al. 2019; Zhang 2020; Xiao et al. 2021). Since 2007, when the first FRB was discovered, there have been a large number of models proposed (e.g., Lyubarsky 2014; Geng & Huang 2015; Dai et al. 2016; Zhang 2017; Yang & Zhang 2018, 2021; Platts et al. 2019). However, the radiation mechanism of FRBs is still unclear. Remarkably, FRB 200 428 was detected in association with an X-ray burst from the Galactic magnetar SGR 1935+2146 (e.g., Bochenek et al. 2020; CHIME/FRB Collaboration et al. 2020; Mereghetti et al. 2020; Li et al. 2021a; Tavani et al. 2021). This indicates that magnetars can be a striking scenario for the origin of FRBs (e.g., Zhang 2020). More interestingly, there are some repeating FRBs showing long periodic activities, e.g., ~ 16.35 days for FRB 180 916.J0158+65 (Chime/Frb Collaboration et al. 2020) and a possible ~ 160 days for FRB 121 102 (Rajwade et al. 2020; Cruces et al. 2021). Many scenarios have been proposed to explain the periodicities (e.g., Smallwood et al. 2019; Beniamini et al. 2020; Dai & Zhong 2020; Gu et al. 2020; Levin et al. 2020; Lyutikov et al. 2020; Deng et al. 2021; Geng et al. 2021; Kuerban et al. 2021; Li & Zanazzi 2021; Wada et al. 2021; Xu et al. 2021), in which a leading one invokes magnetars in high-mass binaries (e.g., Ioka & Zhang 2020; Li et al. 2021b). Therefore, it also becomes a very interesting subject in the FRB field whether magnetars can exist in binary systems (Zhang & Gao 2020). Moreover, some γ -ray binaries are suggested to be magnetar binaries. Torres et al. (2012) reported a magnetar-like X-ray flare from another gamma-ray binary LS I +61° 303. Last year, Yoneda et al. (2020) showed that the gamma-ray binary LS 5039 maybe a magnetar binary, because the obtained spin period and its derivative are similar to those of magnetars. Additionally, the obtained spin-down luminosity is lower than its bolometric luminosity and its emissive energy should be supplied by the decay of the magnetic field of the magnetar.

Popov & Turolla (2012) modeled the formation channel for the NS in the Be/X-ray binary SXP 1062, which has a long spin period ($P_s = 1062$ s) and short age, indicating that its initial magnetic field may be larger than 10^{14} G and decayed to 10^{13} G. Zhang et al. (2004) calculated the spin evolution of NSs in OB/X-ray binaries before steady wind accretion. Shakura et al. (2012) proposed that wind matter around an accreting NS should form a quasi-spherical shell above the magnetosphere rather than directly accreted if the cooling time of the wind plasma is longer than its freefall time. The results of population synthesis (Li et al. 2016) with the subsonic settling accretion (Shakura et al. 2012) are better consistent

with observations. Karino (2020) found that the wind velocity makes a great difference on the spin evolution of NSs in wind-fed HMXBs.

In this paper, we perform the spin evolution of NSs in wind-fed HMXBs and compare the spin period distribution with the observations, aiming to see if there is any difference between old magnetars and other NSs. In Section 2, we describe the wind accretion regimes and Section 3 presents the numerical results as well as the comparison with observations. Finally, our discussion and summary are provided in Sections 4 and 5, respectively.

2. Model

2.1. Wind Accretion Regimes

We consider a wind-fed accretion binary system consisting of an NS of mass $M_{\text{NS}} = 1.4 M_{\odot}$ and a massive main sequence (MS) companion that does not fill its Roche lobe (RL). In general, the NS in a binary system is born with a short spin period ($P_s \sim 0.01\text{--}0.1$ s), and then it can experience the following possible phases sketched in Figure 1.

2.1.1. Phase a: The Pulsar-like Spindown Phase

First, an NS appears as a radio pulsar after its birth in a supernova explosion if its magnetic or radiation pressure is high enough to boot the wind plasma outside the Bondi radius $R_g = 2GM_{\text{NS}}/v_{\text{rel}}^2$ (Bondi & Hoyle 1944) or the radius of the light cylinder $R_{\text{lc}} = cP_s/2\pi$. Here $v_{\text{rel}} = (v_{\text{orb}}^2 + v_w^2)^{1/2}$ is the relative speed toward the NS, where v_{orb} is the NS velocity at the orbit and v_w is the stellar wind velocity. G and c are the gravitational constant and speed of light, respectively. For clarity, we define R_{wind} as the wind termination radius from the NS and $R_{\text{eff}} = \max(R_g, R_{\text{lc}})$ as the effective radius of the NS, so we can get $R_{\text{wind}} > R_{\text{eff}}$ in phase a. The spin-down rate induced by magnetic dipole radiation in this phase is (Zhang et al. 2004)

$$\dot{P}_a = 9.73 \times 10^{-18} \mu_{31}^2 P_0^{-1} I_{45}^{-1} \text{ s s}^{-1}, \quad (1)$$

where μ_{31} and P_0 are the NS's magnetic dipole moment in units of 10^{31} G cm² and its spin period in units of 1 s, respectively. $I = I_{45} \times 10^{45}$ g cm² is the moment of inertia of the NS.

Phase a ends when either the wind material penetrates the light cylinder radius or it enters the Bondi radius, i.e., $R_{\text{wind}} < R_{\text{eff}}$; correspondingly the transitional spin periods P_{ab} and P_{ac} (Davies & Pringle 1981) are

$$P_{\text{ab}} = 0.37 \mu_{31}^{1/3} \dot{M}_{15}^{-1/6} v_8^{-5/6} \left(\frac{M_{\text{NS}}}{M_{\odot}} \right)^{1/3} \text{ s}, \quad (2)$$

and

$$P_{\text{ac}} = 0.38 \mu_{31}^{1/2} \dot{M}_{15}^{-1/4} v_8^{-1/2} \text{ s}, \quad (3)$$

Wind accretion regimes

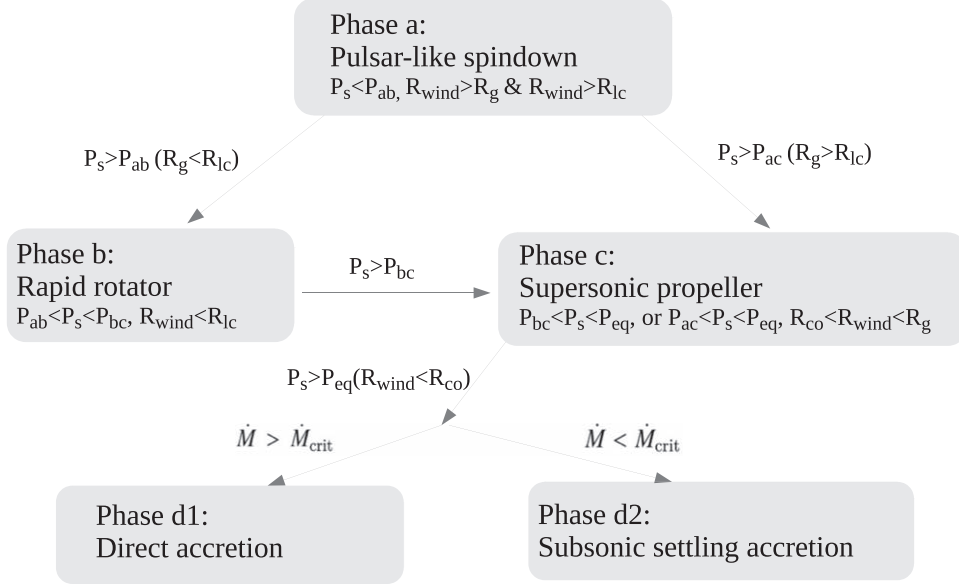


Figure 1. Wind accretion regimes, see Section 2.1.

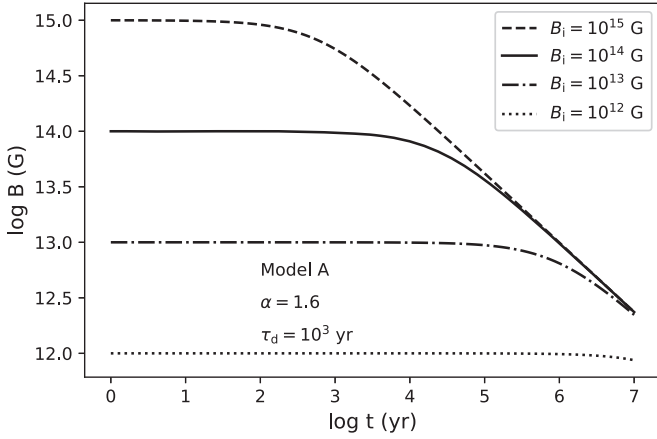


Figure 2. The magnetic field evolution with $B_i = 10^{12}$, $B_i = 10^{13}$, $B_i = 10^{14}$ and $B_i = 10^{15}$ G, where $B < 10^{13}$ G remains unchanged in its life while $B_i \geq 10^{13}$ G decays in the form of Equation (15).

where v_8 is the relative speed toward the NS in units of 10^8 cm s^{-1} and $\dot{M} = \dot{M}_{15} \times 10^{15}$ g s^{-1} is the accretion rate onto the NS given by Bondi & Hoyle (1944)

$$\dot{M} = \pi R_g^2 \rho_w v_{\text{rel}}. \quad (4)$$

Here ρ_w is the stellar wind density at the orbit of the NS, which can be computed by assuming an isotropically expanding wind

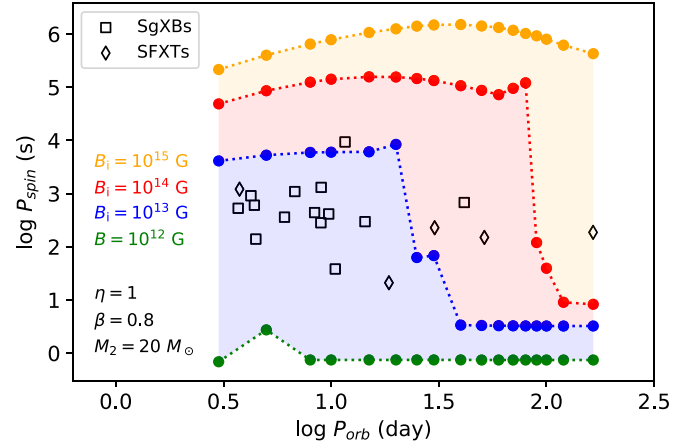


Figure 3. Results of the reference model in the Corbet diagram. The filled circles indicate the maximum spin periods $P_{s,\text{max}}$ during the evolution process in each case. The green, blue, red and orange circles signify that the initial magnetic fields of the NSs are $B_i = 10^{12}$, $B_i = 10^{13}$, $B_i = 10^{14}$ and $B_i = 10^{15}$ G, respectively. The dashed lines string together the circles in the same color and the colored regions give the predicted $P_{s,\text{max}}$ distributions for the NSs with initial magnetic field between the upper and lower dashed lines. The squares and diamonds mark two subclasses of HMXBs, which are SgXBs and SFXTs respectively.

at a speed of v_w

$$\rho_w = -\dot{M}_2 / (4\pi a^2 v_w), \quad (5)$$

where a is the orbital separation of the system and \dot{M}_2 is the mass loss rate of the donor star.

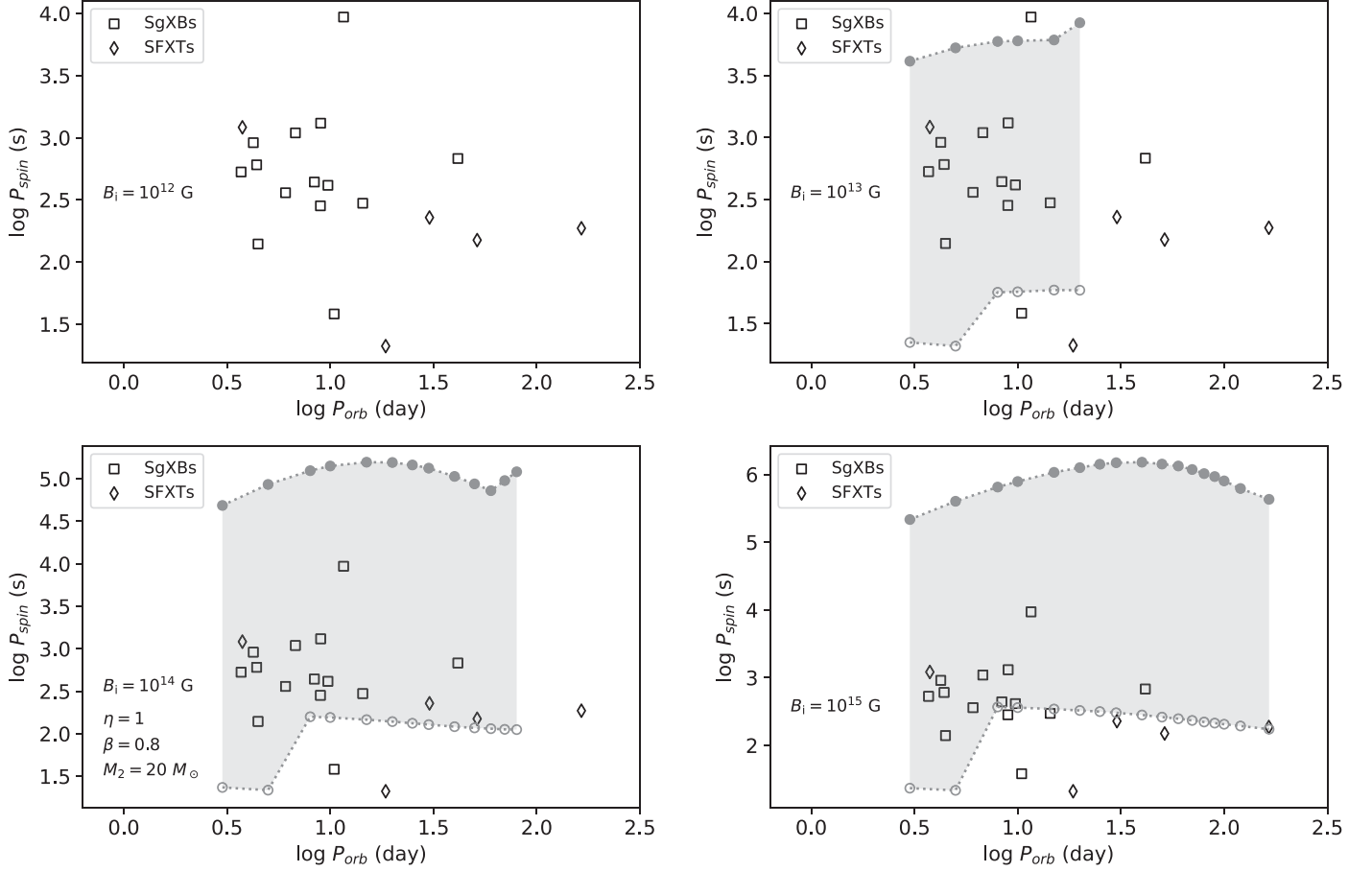


Figure 4. Results of the reference model with NSs' luminosity $L_X > 10^{32}$ erg s^{-1} during the accretion phases. The gray filled and unfilled circles indicate the predicted maximum and minimum P_s of the NSs, respectively. Also, the gray regions give the predicted range of P_s of the NSs in each panel. From top-left to bottom-right panels, the magnetic fields are $B_i = 10^{12}$, $B_i = 10^{13}$, $B_i = 10^{14}$ and $B_i = 10^{15}$ G, respectively. There is no NS that enters accretion phases in the case of $B_i = 10^{12}$ G.

2.1.2. Phase b: The Rapid Rotator Phase

The rapid rotator phase (phase b) comes if the wind material from the donor star enters the light cylinder of the NS in front of the Bondi radius in the weak stellar wind case (Illarionov & Sunyaev 1975), i.e., $R_g < R_{lc}$ in this case and phase b occurs when $R_{wind} < R_{lc}$, as well as $P > P_{ab}$ commences before $P > P_{ac}$ if $P_{ab} < P_{ac}$. The spin-down rate in phase b is (Zhang et al. 2004)

$$\dot{P}_b = 8.59 \times 10^{-17} \mu_{31} \dot{M}_{15}^{1/2} v_8^{5/2} P_0^2 \text{ s s}^{-1}. \quad (6)$$

When the outer boundary of the wind plasma reaches the Bondi radius (i.e., $R_{wind} = R_g$), phase b stops at (Davies & Pringle 1981)

$$P_{bc} = 0.22 \mu_{31} \dot{M}_{15}^{-1/2} v_8^{1/2} \left(\frac{M_{NS}}{M_\odot} \right)^{-1} \text{ s}. \quad (7)$$

2.1.3. Phase c: The Supersonic Propeller Phase

When $R_{wind} < R_g$, which is equivalent to $P > P_{bc}$, the supersonic propeller phase (phase c) arrives in the weak stellar wind case, while NSs will enter phase c directly from phase a if the stellar wind is strong enough (Illarionov & Sunyaev 1975), i.e., phase c comes when $R_{wind} < R_g$ in the case of $R_g > R_{lc}$ as well as $P > P_{ac}$ occurs before $P > P_{ab}$ if $P_{ac} < P_{ab}$. The spin-down rate in this phase is (Zhang et al. 2004)

$$\dot{P}_c = 1.6 \times 10^{-14} \mu_{31}^{8/13} \dot{M}_{15}^{9/13} P_0^{21/13} \text{ s s}^{-1}.$$

When the inner boundary of the wind plasma reaches the corotation radius $R_{co} = (GM/\Omega_s^2)^{1/3}$, phase c ends at the equilibrium spin period (Davies & Pringle 1981)

$$P_{eq} = 5.0 \mu_{31}^{2/3} \dot{M}_{15}^{-1/3} v_8^{-2/3} \text{ s}. \quad (8)$$

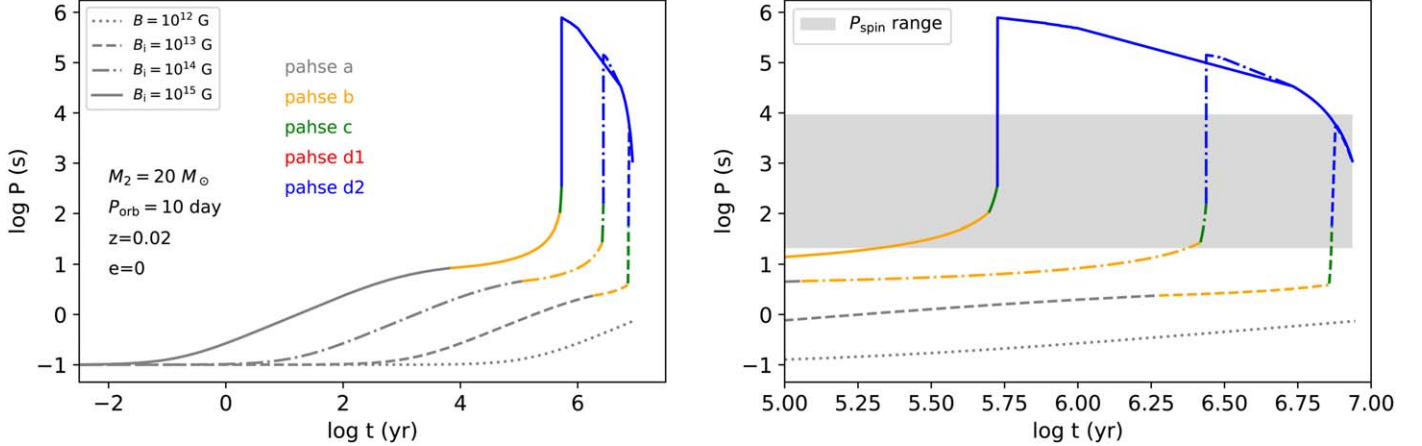


Figure 5. The spin evolution process of the reference model when $P_{\text{orb}} = 10$ days. The dotted, dashed, dotted–dashed and solid lines represent the evolution of NSs with magnetic field $B_i = 10^{12}$, $B_i = 10^{13}$, $B_i = 10^{14}$ and $B_i = 10^{15}$ G, respectively. In each line, the black, orange, green, red and blue parts indicate that the NSs are in phases a, b, c, d1 and d2 respectively. In phase c (the supersonic propeller phase) and d2 (the subsonic settling accretion phase) before it reaches equilibrium, the NS loses angular momentum rapidly so that its spin period rises steeply. The right panel is the magnified part of the left panel with $5 < \log t \text{ (yr)} < 7$ and the gray region covers the P_{spin} range of the NSs in HMXBs.

2.1.4. Phase d1 and Phase d2: The Accretion Phases

When the inner boundary of the wind material becomes smaller than the corotation radius ($R_{\text{wind}} < R_{\text{co}}$) and the cooling is efficient, as indicated by $P_s > P_{\text{eq}}$, a bow shock can form at the Bondi radius around the NS and quasi-spherical accretion onto the NS occurs. The shocked matter falls toward the magnetosphere of the NS at a supersonic speed if it cools down rapidly, or it forms a quasi-static shell around the magnetosphere and settles down subsonically if the matter remains hot, corresponding to the Bondi–Hoyle–Littleton (BHL) accretion phase (phase d1) or the subsonic settling accretion phase (phase d2). Phase d1 takes place at $\dot{M} > \dot{M}_{\text{crit}}$ while phase d2 occurs at $\dot{M} < \dot{M}_{\text{crit}}$ (Shakura et al. 2012), where $\dot{M}_{\text{crit}} = 8.4 \times 10^{15} \mu_{31}^{1/4} (M/M_{\odot})^{-1/2} R_6^{7/8} \text{ g s}^{-1}$ (Arons & Lea 1976a, 1976b; Elsner & Lamb 1977, 1984).

In phase d1, the accreted material transfers spin-up torque to the NS

$$N_{\text{super}} = I \dot{\Omega} = \dot{M} R_M^2 \Omega_S, \quad (9)$$

where $R_M = [\mu^4 / (2GM_{\text{NS}} \dot{M}^2)]^{1/7}$ is the magnetospheric radius. This phase ends at the spin equilibrium state with $P_s = P_{\text{eq}}$. In phase d2, besides the material torque, the interaction between the magnetosphere and the plasma exerts an additional one on the NS. Therefore, the total torque that governs the NS spin evolution is

$$N_{\text{sub}} = A_{\text{const}} \dot{M}_{X,16}^{7/11} - B_{\text{const}} \dot{M}_{X,16}^{3/11}, \quad (10)$$

where

$$A_{\text{const}} \simeq 3.73 \times 10^{31} K_1 \mu_{31}^{1/11} v_8^{-4} \left(\frac{P_{\text{orb}}}{10 \text{ days}} \right)^{-1}, \quad (11)$$

$$B_{\text{const}} \simeq 3.61 \times 10^{31} K_1 \mu_{31}^{13/11} \left(\frac{P_s}{100 \text{ s}} \right)^{-1}. \quad (12)$$

Here $K_1 \sim 40$ is a dimensionless numerical factor (Shakura et al. 2012) and $\dot{M}_{X,16} = \dot{M}_X / 10^{16} \text{ g s}^{-1}$, where $\dot{M}_X = 10^7 \text{ g s}^{-1} \mu_{30}^{2/21} (\dot{M} / 10^{10} \text{ g s}^{-1})^{9/7}$ (Popov et al. 2015). The equilibrium spin period in phase d2, where this phase stops, reads (Li et al. 2016)

$$P_{\text{eq,sub}} \simeq 96.8 \mu_{31}^{12/11} v_8^4 \dot{M}_{16}^{-4/11} \left(\frac{P_{\text{orb}}}{10 \text{ days}} \right) \text{ s}. \quad (13)$$

In observation, the system in accretion phases (phase d1 and phase d2) can be seen in X-ray band if the luminosity is high enough.

2.2. The Evolution of the Binary

We use the binary star evolution (BSE) code (Hurley et al. 2000, 2002; Kiel & Hurley 2006; Shao & Li 2014, 2015, 2021) to simulate the evolution of binary systems. The simulation begins from the birth time of the NS when the optical star is thought to be in the zero age main sequence (ZAMS) stage, and ends when the optical/companion star starts to fill its RL or explodes as a supernova.

One can estimate the wind velocity adopting the standard formula from Castor et al. (1975)

$$v_w = \eta v_{\text{esc}} (1 - R_2/a)^\beta, \quad (14)$$

where $v_{\text{esc}} = \sqrt{2GM_2/R_2}$ is the escape velocity at the surface of the optical star. Here we take the coefficient $\eta \sim 0.5\text{--}3$ and the power law index $\beta \sim 0.8\text{--}7$ (Waters & van Kerkwijk 1989; Owocki 2014; Karino 2020).

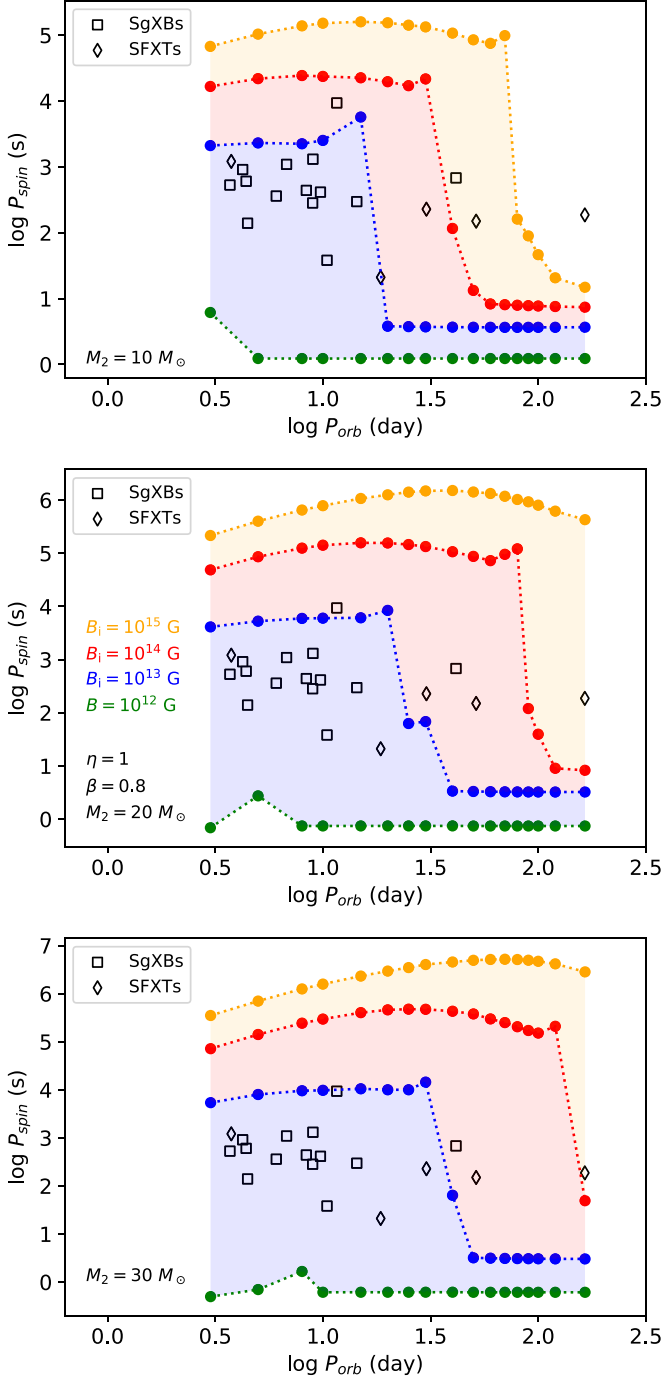


Figure 6. Same as Figure 3 but with the companion mass $M_2 = 10, 20$ (the reference model) and 30 , from top to bottom respectively.

2.3. The Evolution of the Magnetic Field

The magnetic field of an NS decays in the following form (Aguilera et al. 2008; Dall’Osso et al. 2012; Fu & Li 2012)

$$B(t) = B_i(1 + \alpha t/\tau_{d,i})^{-1/\alpha}, \quad (15)$$

where $\alpha = 1.6$ and the initial field decay time $\tau_{d,i} = 10^3 \text{ yr}/(B_i/10^{15} \text{ G})^\alpha$ (Fu & Li 2012) in our reference model. We plot the magnetic field evolution with four initial values in Figure 2, which are $B_i = 10^{12}$, $B_i = 10^{13}$, $B_i = 10^{14}$ and $B_i = 10^{15} \text{ G}$.

3. Results

3.1. The Reference Model

We first consider a series of circular orbital binaries as the reference model, in which each one consists of a $1.4 M_\odot$ NS and a $20 M_\odot$ optical star with metallicity $Z = Z_\odot$. The wind parameters of the companion η and β are set to be 1.0 and 0.8 respectively. Figure 3 features the results of the reference model in the Corbet diagram, where the filled circles indicate the maximum spin periods $P_{s,\text{max}}$ during the evolution process in each case. From lower to upper, the green, blue, red and orange circles signify that the initial magnetic fields of the NSs are $B_i = 10^{12}$, $B_i = 10^{13}$, $B_i = 10^{14}$ and $B_i = 10^{15} \text{ G}$, respectively. From left to right in each color, the circles symbolize the orbital periods of the binaries, which are 3, 5, 8, 10, 15, 20, 25, 30, 40, 50, 60, 70, 80, 90, 100, 120, 165 days, respectively. The dashed lines string together the circles with the same color, predicting the possible $P_{s,\text{max}}$ with the P_{orb} ranging from 3 to 165 days. The colored regions give the predicted $P_{s,\text{max}}$ distributions of the NSs with initial magnetic field between the upper and lower dashed lines. For example, the blue dashed line and region predict the $P_{s,\text{max}}$ of the NSs with $B_i = 10^{13} \text{ G}$ and $10^{12} < B_i \leq 10^{13} \text{ G}$. From this figure, one can ascertain that the NSs with high initial magnetic field and in short orbital period systems can spin down to very slow rotation, because the strong magnetic fields and the small separations make the NS easy to capture stellar wind from the companion. The NSs soon enter phase c or d2 after being captured and quickly lose their angular momentum (see Figure 5). There are significant drops in the blue and red dashed lines but not in the orange and green dashed lines in Figure 3, because cases with $B_i = 10^{12} \text{ G}$ and $B_i = 10^{15} \text{ G}$ end at phases a/b and d2, respectively, while cases with $B_i = 10^{13} \text{ G}$ and $B_i = 10^{14} \text{ G}$ in short orbital period systems end at phase d2 and those in long orbital period systems end at phase a/b. The second green circle ends at phase b while others end at phase a, which leads to a small bump in the green dashed line.⁷

We compare our results with two subclasses of HMXBs with detected P_s and P_{orb} , which are the supergiant X-ray binaries (SgXBs) and the supergiant fast X-ray transients (SFXTs). The triangles and squares mark the SgXBs and SFXTs respectively.⁸ The SgXBs and SFXTs are two subclasses of HMXBs. SgXBs are persistent systems in X-rays ($L_X = 10^{36} - 10^{38} \text{ erg s}^{-1}$),

⁷ This may be a numerical mistake because it jumps from phase a to phase b in the last step. Considering there is no significant influence on the results, we do not discuss it in the following.

⁸ Data from Martínez-Núñez et al. (2017) and Tauris et al. (2017).

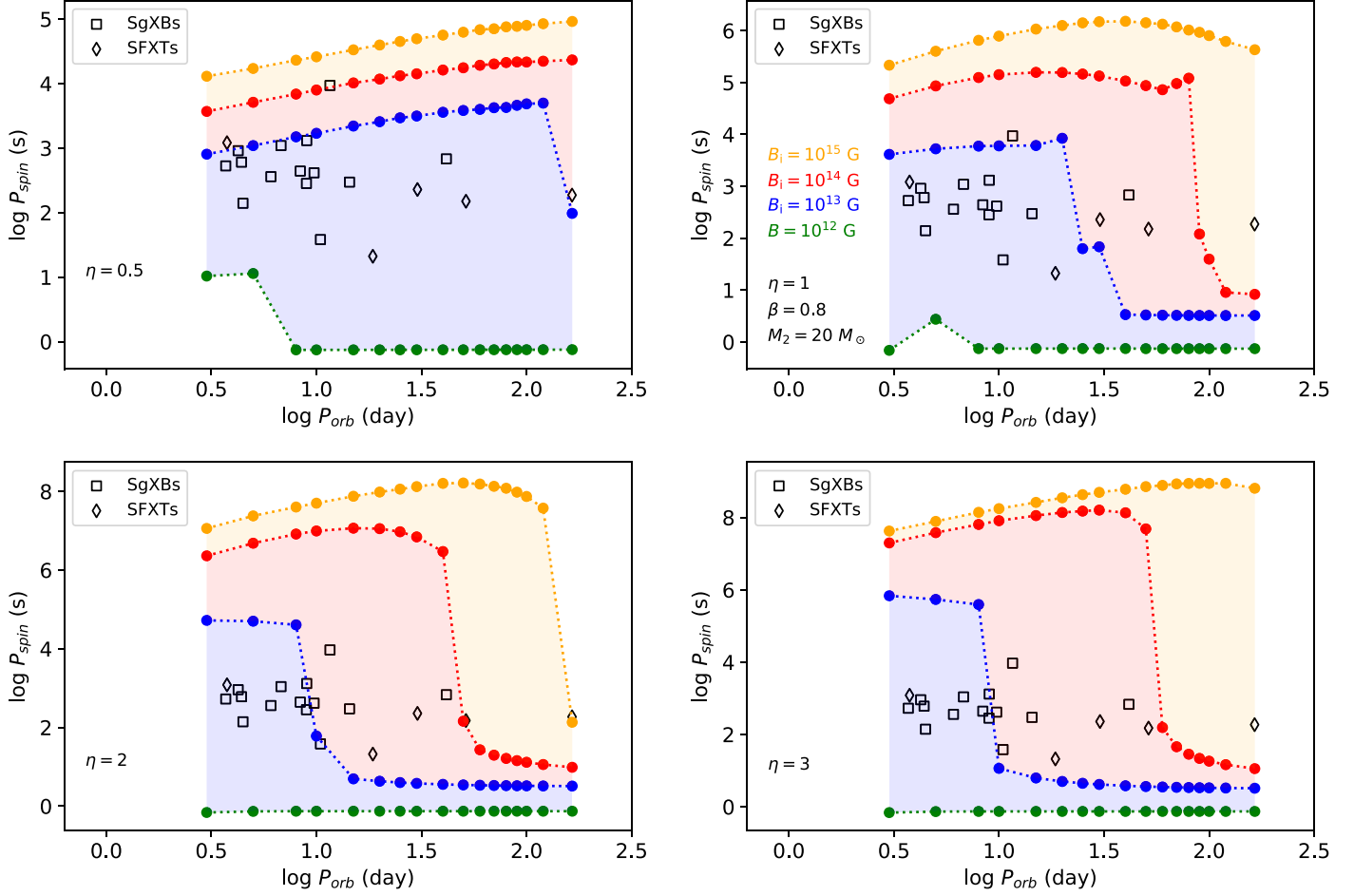


Figure 7. Same as Figure 3 but with the wind coefficient $\eta = 0.5, 1$ (the reference model), 2 and 3 from top-left to bottom-right. Compared with the reference model, there are less sources in the red and orange regions when $\eta = 0.5$, while there are more sources in these regions when $\eta = 2$ or 3. This may imply that the larger the wind coefficient, the more magnetars are in HMXBs.

one of which consists of a compact accretor and a supergiant mass donor of spectral type O8-B1 I/II with strong stellar wind (Martínez-Núñez et al. 2017; Tauris et al. 2017). However, SFXTs are not persistent, which stay in quiescence at $L_X = 10^{32} - 10^{34} \text{ erg s}^{-1}$ for most of the time (Romano et al. 2015) and exhibit short outbursts lasting a few hours reaching $10^{37} - 10^{38} \text{ erg s}^{-1}$ (Rampy et al. 2009; Bozzo et al. 2011). Figure 3 demonstrates that most of the observed HMXBs, which have $P_s < 1000 \text{ s}$ and $P_{\text{orb}} < 30 \text{ days}$, are distributed in the blue region, meaning that they are probably normal NSs. Five other sources with $P_s > 1000 \text{ s}$ or $P_{\text{orb}} > 30 \text{ days}$ are in the red or orange regions, indicating that they may have strong magnetic fields. One of them is in the orange region, which is probably a magnetar. The red dashed line can be seen as the separatrix between magnetars and other NSs.

Figure 4 displays the P_s regions of NSs' luminosity $L_X > 10^{32} \text{ erg s}^{-1}$ during the accretion phases. The gray filled and unfilled circles indicate the predicted maximum and

minimum P_s of the NSs, respectively. The gray regions also give the predicted range of P_s for the NSs in each panel. From top-left to bottom-right panels, the magnetic fields are $B_i = 10^{12}, B_i = 10^{13}, B_i = 10^{14}$ and $B_i = 10^{15} \text{ G}$, respectively. In the case of $B_i = 10^{12} \text{ G}$, no NS enters the accretion phase.

We plot the spin evolution process of the reference model with $P_{\text{orb}} = 10 \text{ days}$ in Figure 5. From lower to upper, the dotted, dashed, dotted-dashed and solid lines represent the evolution of NSs with magnetic field $B_i = 10^{12}, B_i = 10^{13}, B_i = 10^{14}$ and $B_i = 10^{15} \text{ G}$, respectively. In each line, the black, orange, green, red and blue parts indicate that the NSs are in phases a, b, c, d1 and d2, respectively. The right panel is the magnified part of the left panel with $5 < \log t \text{ (yr)} < 7$.

3.2. Parameter Study

The main configurable parameters in our model are the companion mass M_2 , and the wind parameters η and β . In this

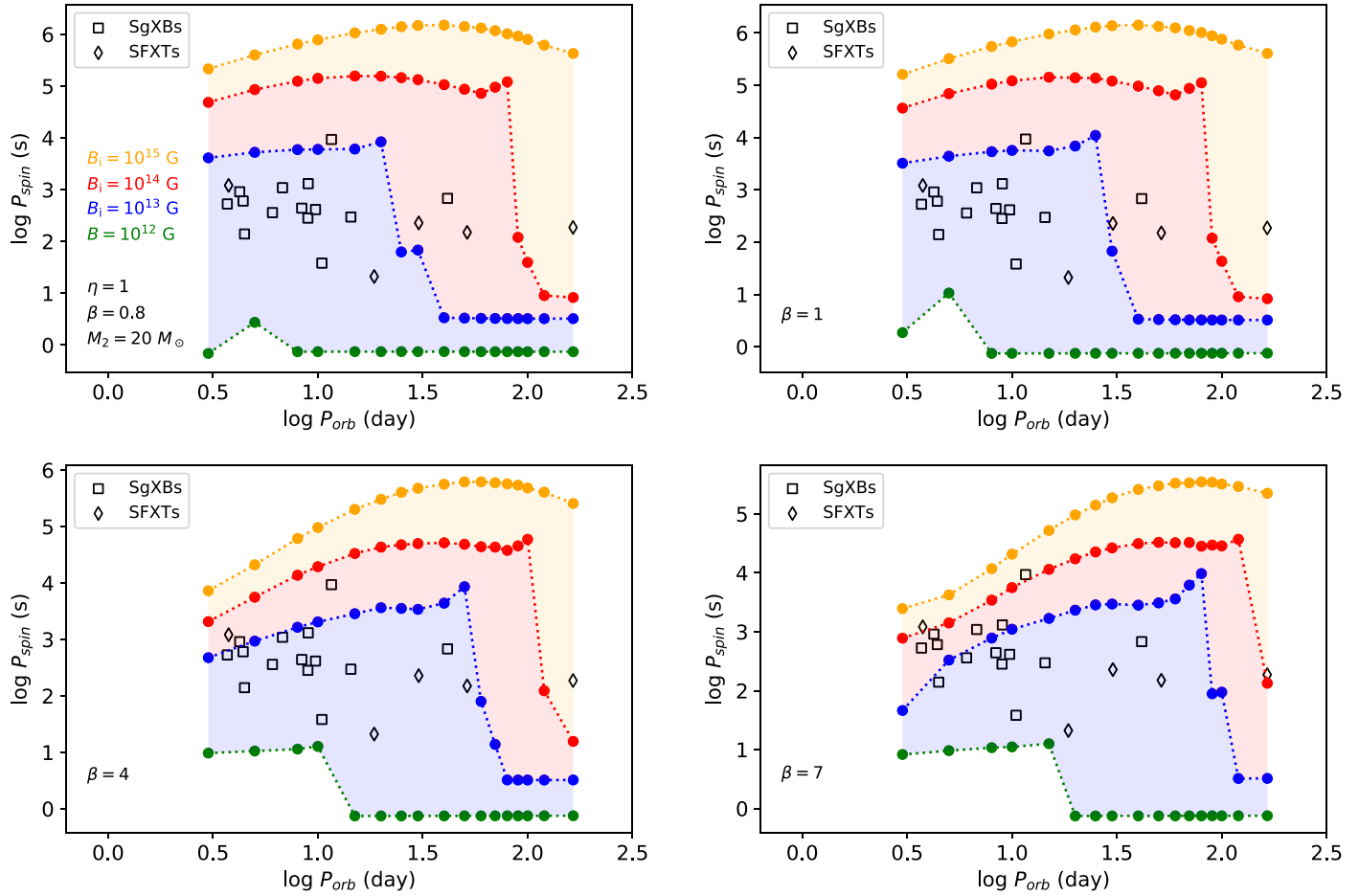


Figure 8. Same as Figure 3 but with the wind power index $\beta = 0.8$ (the reference model), 1, 4 and 7 from top-left to bottom-right. It shows that when β is much larger, some sources with short orbital periods need stronger magnetic fields to explain their long spin periods.

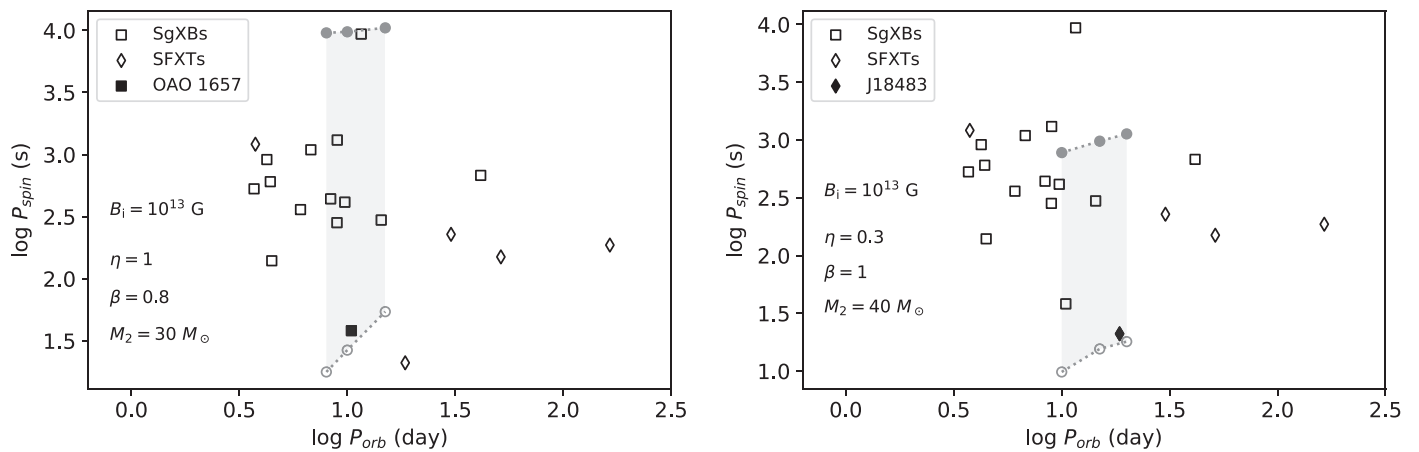


Figure 9. Parameters that can cover OAO 1657 (left) and J18483 (right).

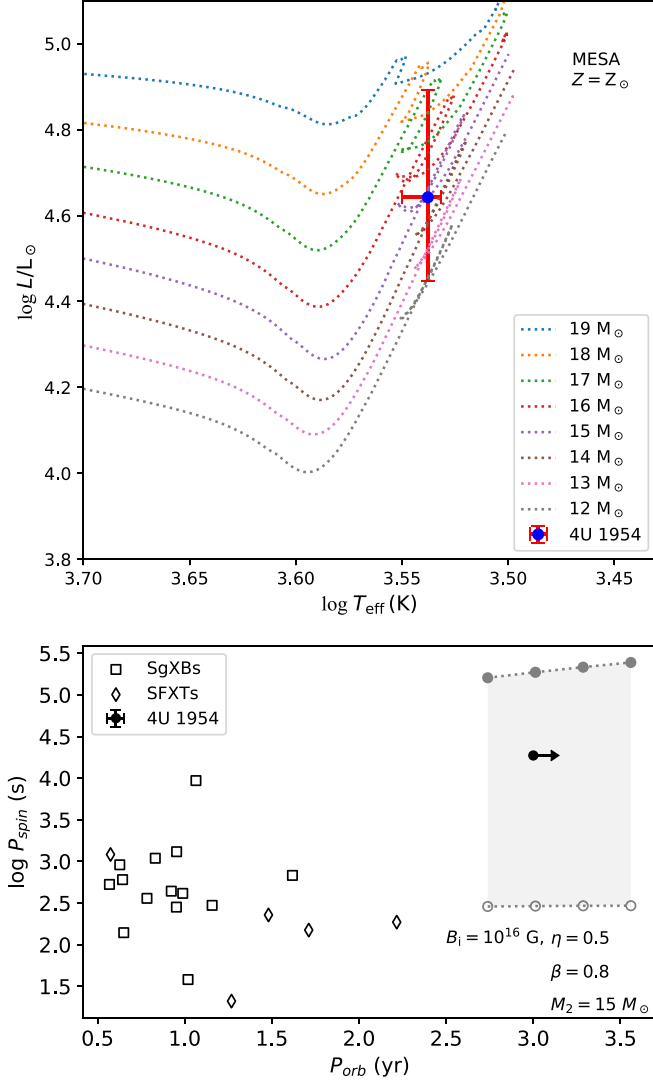


Figure 10. Upper: Location of the companion of 4U 1954 on the HRD. Lower: A group of parameters that can cover 4U 1954, in which the initial magnetic field is $B_i = 10^{16} \text{ G}$.

subsection, we vary these parameters based on the reference model to see how they can influence the results.

3.2.1. The Companion Mass M_2

We first change the mass of the companion M_2 . The results of maximum spin period with different companion mass are exhibited in Figure 6. From top to bottom, M_2 is taken to be $10 M_{\odot}$, $20 M_{\odot}$ (the reference model) and $30 M_{\odot}$ respectively. It shows that more sources fall in the red and orange regions in the upper panel while less sources are in these regions in the lower panel compared with the reference model. This may imply that systems with less massive companions are more likely to dedicate HMXBs with magnetars.

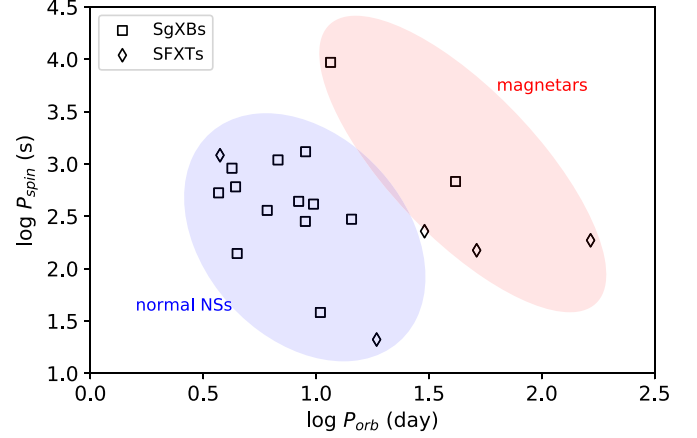


Figure 11. The distribution of magnetars and normal NSs in HMXBs predicted by our model.

3.2.2. The Wind Coefficient η

Figure 7 shows the dependence of P_{max} on the wind coefficient η , where $\eta = 0.5, 1$ (the reference model), 2 and 3 from top-left to bottom-right. Compared with the reference model, we find that less sources are in the red and orange regions when $\eta = 0.5$, while more sources are in these regions when $\eta = 2$ or 3. This may imply that the larger the wind coefficient, the more magnetars are in HMXBs.

3.2.3. The Wind Power Law Index β

Karino (2020) discussed the influence of parameter β within larger scale, where $\beta = 1$ and 7 indicate the fast and slow wind cases, respectively. They found that the NSs spin down rapidly in the slow wind cases due to the propeller effect and settling accretion shell, while magnetic inhibition causes spin-down in the fast cases. Figure 8 presents the P_{max} results with different values of wind power law index β . From top-left to bottom-right, we take $\beta = 0.8$ (the reference model), 1, 4 and 7. It shows that when β is much larger, some sources with short orbital periods need strong magnetic fields to explain their long spin periods, but we are not sure whether β can be as large as 7. This may indicate that in the slow wind cases (Karino 2020), an NS needs a strong magnetic field to get a large R_{lc} to start the interaction with the wind material.

4. Discussion

4.1. Special Sources

4.1.1. J11215–5952

From Figures 3, 7 and 8, we know that only one source is always in the red or orange regions, which is J11215–5952 (hereafter J11215) with orbital period $P_{\text{orb}} = 164.6$ days

and spin period $P_s = 186.78$ s (Masetti et al. 2006; Sidoli et al. 2006, 2007, 2020). That means J11215 needs an initial magnetic field $B_i > 10^{13}$ G to explain its orbital and spin period, which implies that it is probably a magnetar. In a widely-separated binary, the NS may need a large effective radius to let the wind be captured. So, J11215 needs a strong magnetic field to get a long spin period as well as a large R_{lc} in phase a.

4.1.2. OAO 1657–415 and J18483–0311

There are two sources not covered in Figure 4 because their spin periods are too small, which are OAO 1657–415 (hereafter OAO 1657) with $P_{orb} = 10.448$ days and $P_s = 38.2$ s and J18483–0311 (hereafter J18483) with $P_{orb} = 18.55$ days and $P_s = 21$ s.⁹ We think these sources are or have been in the direct accretion phase (phase d1) so that they can spin up to a very fast rotation. We show two groups of parameters that can cover OAO 1657 and J18483 in Figure 9, in which we can explain OAO 1657 within the parameter space in our model while J18483 needs a small η and massive companion.

4.1.3. 4U 1954+31

Recently, 4U 1954+31 has been re-classified as an HMXB containing a late-type supergiant with mass of $9_{-2}^{+6} M_\odot$ (Hinkle et al. 2020). However, the companion mass, ascertained according to its position in the Hertzsprung–Russell Diagram (HRD), is model dependent, as there are still many uncertainties that plague the evolutionary tracks of stars, for instance the stellar wind and mixing. As a comparison, we also evolve some models using the stellar evolutionary code Modules for Experiments in Stellar Astrophysics (MESA) (Paxton et al. 2011) and compare their evolutionary tracks with 4U 1954+31 in HRD (the upper panel of Figure 10). In our models, the convection is calculated following the standard mixing-length theory (Böhm 1958) with the scale parameter $\alpha_{MLT} = 1.5$, and the convective regions are determined by the Ledoux criterion. The semi-convection parameter is assumed to be $\alpha_{SC} = 1.0$. In addition, the mass loss due to stellar wind is calculated according to their effective temperature and surface hydrogen (H) mass fraction. That is, the prescriptions of Vink et al. (2001) and Nugis & Lamers (2000) are used for hot H-rich ($T_{eff} > 10^4$ K and $X_s \geq 0.4$) and H-poor ($T_{eff} > 10^4$ K and $X_s < 0.4$) stars, respectively. While for $T_{eff} < 10^4$ K we change to that of de Jager et al. (1988). We simulate their evolution from ZAMS to core-carbon (C) ignition, with initial mass M_i ranging from 12 to 19 M_\odot . Our predicted mass of 4U 1954+31 is $15_{-3}^{+3} M_\odot$, which is $\sim 6 M_\odot$ heavier than that of Hinkle et al. (2020). The spin period of the NS is ~ 5 hr (Corbet et al. 2008; Marcu et al. 2011; Enoto et al. 2014) while the orbital period is not

confirmed. Only a lower limit of 3 yr is given (Hinkle et al. 2020), which is much longer than the orbital periods of SgXBs and SFXTs in Figure 3. We cannot explain it within the parameter space used above, but the results in the lower panel of Figure 10 can cover it with the following parameters: $\eta = 0.5$, $\beta = 0.8$, $B_i = 10^{16}$ G and $M_2 = 15 M_\odot$. Since the separation of this system is very wide, another possible model to explain its long spin period is that the NS is first spun down by a fallback disk and then interacts with the wind material.

4.2. The Distribution of NSs in HMXBs

Figure 11 depicts the predicted distribution of magnetars and normal magnetic field NSs in HMXBs. In the Corbet diagram, the normal NSs may be centered at the region where the spin periods and orbital periods are both short, while magnetars may be located at the region where either P_s or P_{orb} are long. As proposed in Li & van den Heuvel (1999), the reason is that a strong magnetic field makes an NS achieve a slower spin period in phase a by magnetic dipole radiation, as well as a larger effective radius, so that it is easy for the NS to capture the wind stellar material and it can enter the interaction phases (phase b, c, d1 and d2) earlier, then the interaction between the wind material and the magnetosphere could have a long time to spin the NS down.

5. Summary

In this work, we explore the possible parameter space for magnetars in HMXBs by performing spin evolution of NSs. We arrange and simplify the wind accretion regimes taking the direct and subsonic settling accretion into account. Compared with previous studies, we use grid methods combining the individual and population synthesis method and simulate a more complete evolution process, including the evolution of winds from the companions and the decay of the magnetic fields of the NSs. Our results show that some NSs in the right and upper region in the Corbet diagram, which are in widely-separated systems or have long spin periods, need magnetic fields in magnetar magnitude to reproduce their relatively long spin periods. This implies that some NSs may be born as magnetars in HMXBs, then their magnetic fields decay to the order of normal NSs through a few Myr, but the spin periods record their evolution information and can provide some traces about their initial magnetic fields.

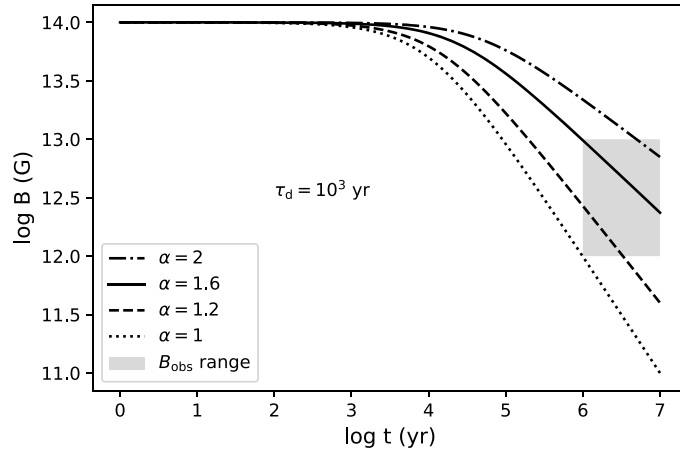
In the calculations we employ the magnetic field evolution model modified by Fu & Li (2012), where the parameters are taken as $\alpha = 1.6$ and $\tau_{d,i} = 10^3 \text{ yr} / (B_i / 10^{15} \text{ G})^\alpha$. There are some debates on these parameters (Dall’Osso et al. 2012; Fu & Li 2012; Gullón et al. 2014) and we study them in the Appendix. The simple β -velocity law used in our work may not accurately describe the wind profile of the companion since some self-consistent calculations indicate that the wind velocity field is more complicated (Gräfener & Hamann 2005, 2008; Sander et al. 2015). We model circular orbits only in the calculations while most of the HMXBs have eccentric orbits because the NSs receive

⁹ The pulsation at 21 s was not confirmed in other observations and a reanalysis of the observations of the discovery showed the lack of any signal (Ducci et al. 2013).

a natal kick at the moment of their formation. The separation becomes variable in eccentric orbits, which leads to more complicated parameters, including the wind velocity, wind density, accretion rate, NS orbital velocity and so on. Because the orbital period is far shorter than the lifetime of the system, for simplicity, we can use a circular orbit to replace the influence of an eccentric orbit and there is no significant impact on the results.

Acknowledgments

We thank the anonymous referee for helpful comments and suggestions. This work was supported by the Natural Natural Science Foundation of China (NSFC, Grant Nos. 11933004, 11988101, 12041301, 12063001, 11773015), Project funded by China Postdoctoral Science Foundation No. 2021M703168, Project U1838201 supported by NSFC and CAS, the program A for Outstanding PhD candidate of Nanjing University, the National Key Research and Development Program of China (2016YFA0400803) and the Fundamental Research Funds for the Central Universities.



Appendix Parameter Study of the Evolution of the Magnetic Field

We take $\alpha = 1.6$ and $\tau_{d,i} = \tau_d / (B_i / 10^{15} \text{ G})^\alpha$ in the reference model, where $\tau_d = 10^3 \text{ yr}$. There are some debates on the range of α , e.g., Dall'Osso et al. (2012) take $0 \leq \alpha \leq 2$ while Fu & Li (2012) think $1.5 \lesssim \alpha \lesssim 1.8$ is most likely. We plot the magnetic field and spin evolution tracks with different α and τ_d in Figures A1 and A2, where the gray region covers the range of the estimated magnetic fields (Caballero & Wilms 2012) and ages of NSs in HMXBs from observations. They show in the cases with large α and τ_d , which mean the magnetic fields evolve slowly, and the NSs can spin down to long periods. The results of the longest spin periods with different α and τ_d are exhibited in Figures A3 and A4, respectively. They demonstrate that more NSs need strong magnetic fields to explain their long spin periods in the rapid evolution cases (with small α and τ_d), while in the slow evolution cases, a magnetar model is dispensable for the observed sources.

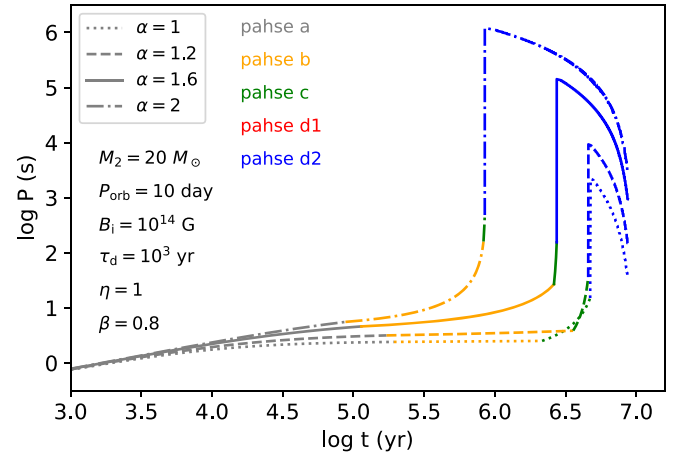


Figure A1. The magnetic field (left) and spin (right) evolution tracks with different α . The gray region in the left panel covers the range of the estimated magnetic field and age of NSs in HMXBs from observations.

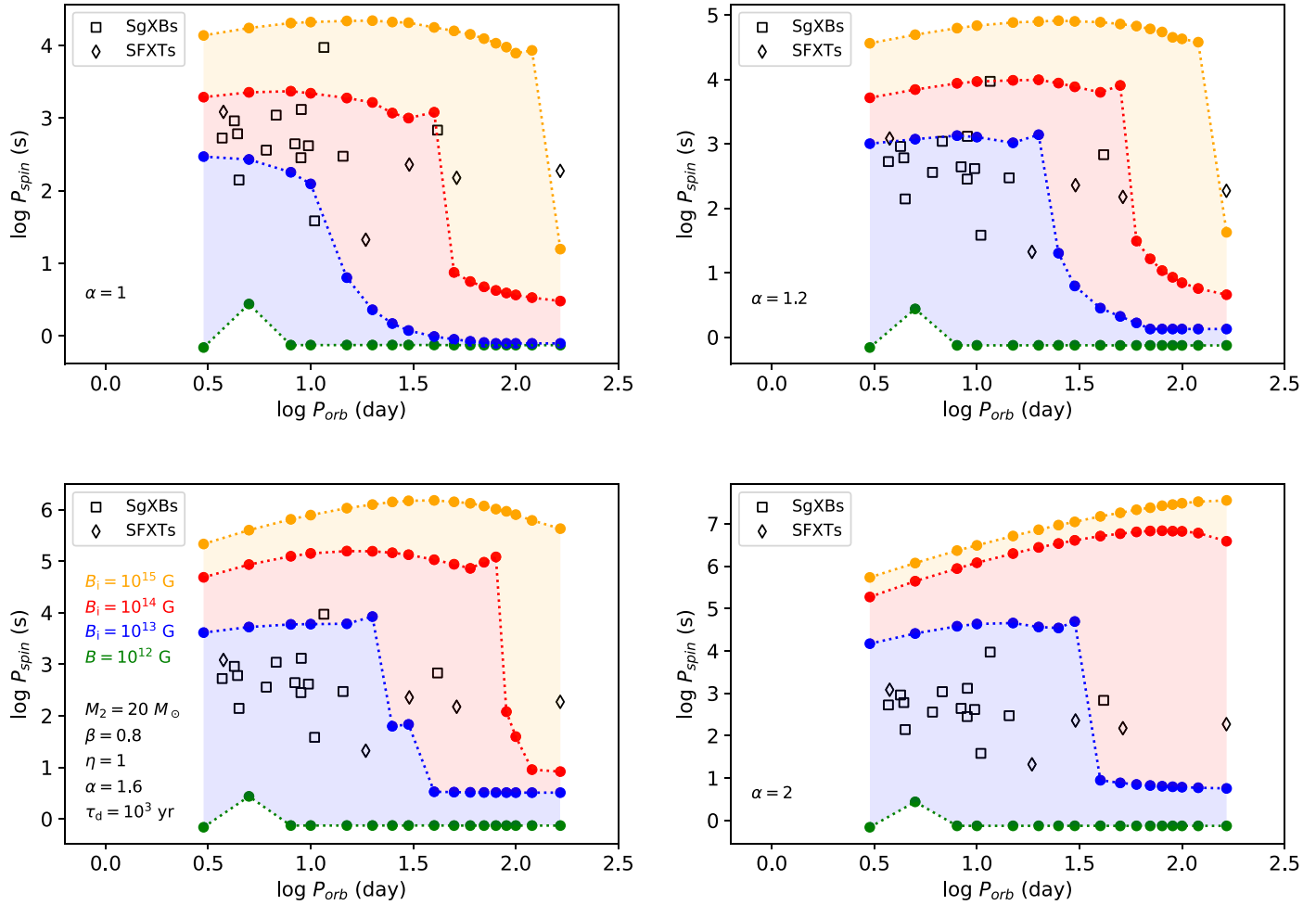


Figure A2. The magnetic field (left) and spin (right) evolution tracks with different τ_d . The gray region in the left panel covers the range of the estimated magnetic field and age of NSs in HMXBs from observations.

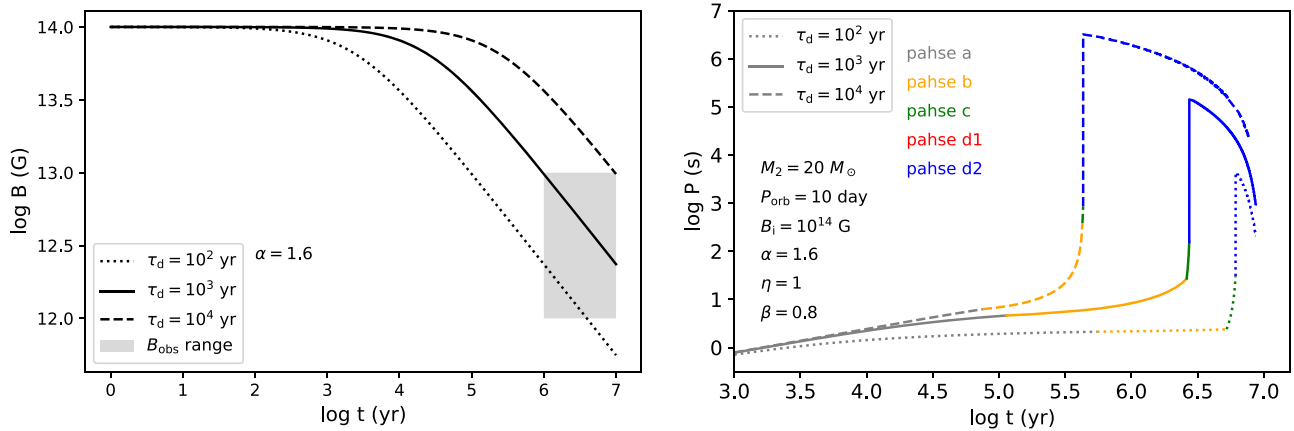


Figure A3. Same as Figure 3 but with $\alpha = 1, 1.2, 1.6$ (the reference model) and 2 from top-left to bottom-right.

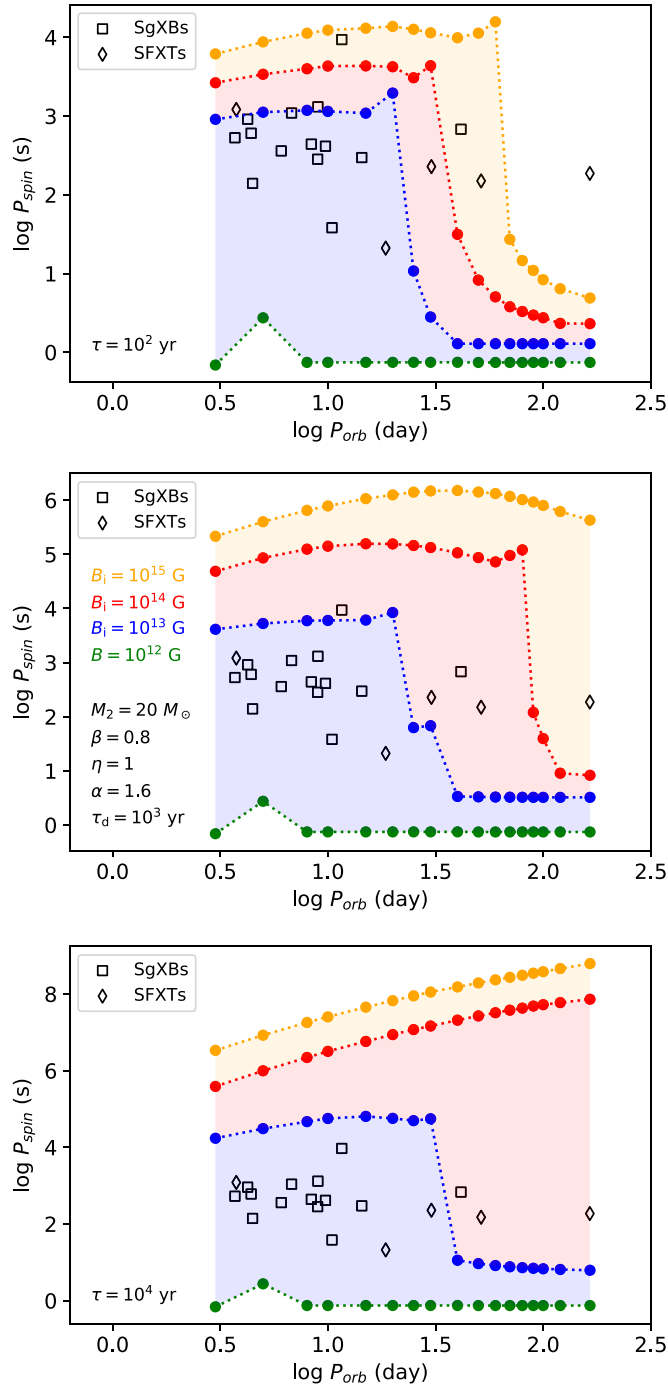


Figure A4. Same as Figure 3 but with $\tau_d = 10^2$, 10^3 (the reference model) and 10^4 yr, from top to bottom.

ORCID iDs

Kun Xu <https://orcid.org/0000-0002-9739-8929>
 Xiang-Dong Li <https://orcid.org/0000-0002-0584-8145>
 Zhe Cui <https://orcid.org/0000-0001-8311-0608>
 Qiao-Chu Li <https://orcid.org/0000-0003-0855-3649>

Xilong Liang <https://orcid.org/0000-0001-9283-8334>
 Jifeng Liu <https://orcid.org/0000-0002-1250-8413>

References

- Aguilera, D. N., Pons, J. A., & Miralles, J. A. 2008, *A&A*, 486, 255
 An, H., & Archibald, R. 2019, *ApJL*, 877, L10
 Arons, J., & Lea, S. M. 1976a, *ApJ*, 210, 792
 Arons, J., & Lea, S. M. 1976b, *ApJ*, 207, 914
 Bachetti, M., Harrison, F. A., Walton, D. J., et al. 2014, *Natur*, 514, 202
 Beniamini, P., Hotokezaka, K., van der Horst, A., & Kouveliotou, C. 2019, *MNRAS*, 487, 1426
 Beniamini, P., Wadiasingh, Z., & Metzger, B. D. 2020, *MNRAS*, 496, 3390
 Bochenek, C. D., Ravi, V., Belov, K. V., et al. 2020, *Natur*, 587, 59
 Böhm, K. H. 1958, *ZAp*, 46, 245
 Bondi, H., & Hoyle, F. 1944, *MNRAS*, 104, 273
 Bozzo, E., Giunta, A., Cusumano, G., et al. 2011, *A&A*, 531, A130
 Caballero, I., & Wilms, J. 2012, *MmSAI*, 83, 230
 Castor, J. I., Abbott, D. C., & Klein, R. I. 1975, *ApJ*, 195, 157
 Chen, W.-C. 2017, *MNRAS*, 465, L6
 Chime/Frb Collaboration, Amiri, M., Andersen, B. C., et al. 2020, *Natur*, 582, 351
 Chime/Frb Collaboration, Andersen, B. C., Bandura, K. M., et al. 2020, *Natur*, 587, 54
 Corbet, R. H. D., Sokoloski, J. L., Mukai, K., Markwardt, C. B., & Tueller, J. 2008, *ApJ*, 675, 1424
 Cordes, J. M., & Chatterjee, S. 2019, *ARA&A*, 57, 417
 Cruces, M., Spitler, L. G., Scholz, P., et al. 2021, *MNRAS*, 500, 448
 Dai, Z. G., Wang, J. S., Wu, X. F., & Huang, Y. F. 2016, *ApJ*, 829, 27
 Dai, Z. G., & Zhong, S. Q. 2020, *ApJL*, 895, L1
 Dall’Osso, S., Granot, J., & Piran, T. 2012, *MNRAS*, 422, 2878
 Dall’Osso, S., Perna, R., & Stella, L. 2015, *MNRAS*, 449, 2144
 Davies, R. E., & Pringle, J. E. 1981, *MNRAS*, 196, 209
 de Jager, C., Nieuwenhuijzen, H., & van der Hucht, K. A. 1988, *A&AS*, 72, 259
 De Luca, A., Caraveo, P. A., Mereghetti, S., Tiengo, A., & Bignami, G. F. 2006, *Sci*, 313, 814
 Deng, C.-M., Zhong, S.-Q., & Dai, Z.-G. 2021, *ApJ*, 922, 98
 Ducci, L., Doroshenko, V., Sasaki, M., et al. 2013, *A&A*, 559, A135
 Duncan, R. C., & Thompson, C. 1992, *ApJL*, 392, L9
 Eksi, K. Y., Andac, I. C., Cikintoglu, S., et al. 2015, *MNRAS*, 448, L40
 Elsner, R. F., & Lamb, F. K. 1977, *ApJ*, 215, 897
 Elsner, R. F., & Lamb, F. K. 1984, *ApJ*, 278, 326
 Enoto, T., Sasano, M., Yamada, S., et al. 2014, *ApJ*, 786, 127
 Fu, L., & Li, X.-D. 2012, *ApJ*, 757, 171
 Geng, J., Li, B., & Huang, Y. 2021, *The Innovation*, 2, 100152
 Geng, J. J., & Huang, Y. F. 2015, *ApJ*, 809, 24
 Gräfener, G., & Hamann, W. R. 2005, *A&A*, 432, 633
 Gräfener, G., & Hamann, W. R. 2008, *A&A*, 482, 945
 Gu, W.-M., Yi, T., & Liu, T. 2020, *MNRAS*, 497, 1543
 Gullón, M., Miralles, J. A., Viganò, D., & Pons, J. A. 2014, *MNRAS*, 443, 1891
 Hinkle, K. H., Lebzelter, T., Fekel, F. C., et al. 2020, *ApJ*, 904, 143
 Ho, W. C. G., & Andersson, N. 2017, *MNRAS*, 464, L65
 Hurley, J. R., Pols, O. R., & Tout, C. A. 2000, *MNRAS*, 315, 543
 Hurley, J. R., Tout, C. A., & Pols, O. R. 2002, *MNRAS*, 329, 897
 Igoshev, A. P., & Popov, S. B. 2018, *MNRAS*, 473, 3204
 Illarionov, A. F., & Sunyaev, R. A. 1975, *A&A*, 39, 185
 Ioka, K., & Zhang, B. 2020, *ApJL*, 893, L26
 Karino, S. 2020, *PASJ*, 72, 95
 Kaspi, V. M., & Beloborodov, A. M. 2017, *ARA&A*, 55, 261
 Kiel, P. D., & Hurley, J. R. 2006, *MNRAS*, 369, 1152
 King, A., & Lasota, J.-P. 2019, *MNRAS*, 485, 3588
 Kluzniak, W., & Lasota, J. P. 2015, *MNRAS*, 448, L43
 Kuerban, A., Huang, Y.-F., Geng, J.-J., et al. 2021, arXiv:2102.04264
 Levin, Y., Beloborodov, A. M., & Bransgrove, A. 2020, *ApJL*, 895, L30
 Li, C. K., Lin, L., Xiong, S. L., et al. 2021a, *NatAs*, 5, 378
 Li, D., & Zanazzi, J. J. 2021, *ApJL*, 909, L25
 Li, Q.-C., Yang, Y.-P., Wang, F. Y., et al. 2021b, *ApJL*, 918, L5

- Li, T., Shao, Y., & Li, X.-D. 2016, *ApJ*, 824, 143
- Li, X. D., & van den Heuvel, E. P. J. 1999, *ApJL*, 513, L45
- Lyubarsky, Y. 2014, *MNRAS*, 442, L9
- Lyutikov, M., Barkov, M. V., & Giannios, D. 2020, *ApJL*, 893, L39
- Marcu, D. M., Fürst, F., Pottschmidt, K., et al. 2011, *ApJL*, 742, L11
- Martínez-Núñez, S., Kretschmar, P., Bozzo, E., et al. 2017, *SSRv*, 212, 59
- Masetti, N., Pretorius, M. L., Palazzi, E., et al. 2006, *A&A*, 449, 1139
- Mereghetti, S., Savchenko, V., Ferrigno, C., et al. 2020, *ApJL*, 898, L29
- Nugis, T., & Lamers, H. J. G. L. M. 2000, *A&A*, 360, 227
- Olausen, S. A., & Kaspi, V. M. 2014, *ApJS*, 212, 6
- Owocki, S. 2014, arXiv:1409.2084
- Paxton, B., Bildsten, L., Dotter, A., et al. 2011, *ApJS*, 192, 3
- Petroff, E., Hessels, J. W. T., & Lorimer, D. R. 2019, *A&ARv*, 27, 4
- Platts, E., Weltman, A., Walters, A., et al. 2019, *PhR*, 821, 1
- Popov, S. B., Postnov, K. A., & Shakura, N. I. 2015, *MNRAS*, 447, 2817
- Popov, S. B., & Turolla, R. 2012, *MNRAS*, 421, L127
- Rajwade, K. M., Mickaliger, M. B., Stappers, B. W., et al. 2020, *MNRAS*, 495, 3551
- Rampy, R. A., Smith, D. M., & Negueruela, I. 2009, *ApJ*, 707, 243
- Rea, N., Esposito, P., Turolla, R., et al. 2010, *Sci*, 330, 944
- Romano, P., Bozzo, E., Mangano, V., et al. 2015, *A&A*, 576, L4
- Sander, A., Shenar, T., Hainich, R., et al. 2015, *A&A*, 577, A13
- Sanjurjo-Ferrín, G., Torrejón, J. M., Postnov, K., et al. 2017, *A&A*, 606, A145
- Shakura, N., Postnov, K., Kochetkova, A., & Hjalmarsdotter, L. 2012, *MNRAS*, 420, 216
- Shao, Y., & Li, X.-D. 2014, *ApJ*, 796, 37
- Shao, Y., & Li, X.-D. 2015, *ApJ*, 802, 131
- Shao, Y., & Li, X.-D. 2021, *ApJ*, 920, 81
- Sidoli, L., Paizis, A., & Mereghetti, S. 2006, *A&A*, 450, L9
- Sidoli, L., Postnov, K., Tiengo, A., et al. 2020, *A&A*, 638, A71
- Sidoli, L., Romano, P., Mereghetti, S., et al. 2007, *A&A*, 476, 1307
- Smallwood, J. L., Martin, R. G., & Zhang, B. 2019, *MNRAS*, 485, 1367
- Tauris, T. M., Kramer, M., Freire, P. C. C., et al. 2017, *ApJ*, 846, 170
- Tavani, M., Casentini, C., Ursi, A., et al. 2021, *NatAs*, 5, 401
- Tong, H. 2015, *RAA*, 15, 517
- Tong, H., & Wang, W. 2019, *MNRAS*, 482, 4956
- Tong, H., Wang, W., Liu, X. W., & Xu, R. X. 2016, *ApJ*, 833, 265
- Tong, H., & Xu, R. X. 2012, *ApJL*, 757, L10
- Torres, D. F., Rea, N., Esposito, P., et al. 2012, *ApJ*, 744, 106
- Tsygankov, S. S., Mushtukov, A. A., Suleimanov, V. F., & Poutanen, J. 2016, *MNRAS*, 457, 1101
- Turolla, R., Zane, S., Pons, J. A., Esposito, P., & Rea, N. 2011, *ApJ*, 740, 105
- Turolla, R., Zane, S., & Watts, A. L. 2015, *PPS*, 78, 116901
- Vink, J. S., de Koter, A., & Lamers, H. J. G. L. M. 2001, *A&A*, 369, 574
- Wada, T., Ioka, K., & Zhang, B. 2021, *ApJ*, 920, 54
- Waters, L. B. F. M., & van Kerkwijk, M. H. 1989, *A&A*, 223, 196
- Xiao, D., Wang, F., & Dai, Z. 2021, *SCPMA*, 64, 249501
- Xu, K., Li, Q.-C., Yang, Y.-P., et al. 2021, *ApJ*, 917, 2
- Xu, K., & Li, X.-D. 2017, *ApJ*, 838, 98
- Xu, K., & Li, X.-D. 2019, *ApJ*, 877, 138
- Yang, Y.-P., & Zhang, B. 2018, *ApJ*, 868, 31
- Yang, Y.-P., & Zhang, B. 2021, *ApJ*, 919, 89
- Yoneda, H., Makishima, K., Enoto, T., et al. 2020, *PhRvL*, 125, 111103
- Zhang, B. 2017, *ApJL*, 836, L32
- Zhang, B. 2020, *Natur*, 587, 45
- Zhang, F., Li, X.-D., & Wang, Z.-R. 2004, *ChJAA*, 4, 320
- Zhang, X., & Gao, H. 2020, *MNRAS*, 498, L1
- Zhou, P., Chen, Y., Li, X.-D., et al. 2014, *ApJL*, 781, L16